Article

Stress Transfer Mechanism of Flange in Split Hopkinson Tension Bar

Hyunho Shin [1,*] , Sanghoon Kim [2] and Jong-Bong Kim [3]

[1] Mechanics of Materials and Design Laboratory, Department of Materials Engineering, Gangneung-Wonju National University, 7 Jugheon-ghil, Gangneung, Gangwon-do 25457, Korea

[2] Laboratory of Solid Properties, Modelling, and Simulation, Department of Mechanical Design and Engineering, Chonnam National University, 50 Daehak-ro, Yeosu, Jeonnam 59626, Korea; shkim83@jnu.ac.kr

[3] Computational Mechanics and Design Laboratory, Department of Mechanical and Automotive Engineering, Seoul National University of Science and Technology, 232 Gongneung-ro, Nowon-gu, Seoul 01811, Korea; jbkim@seoultech.ac.kr

* Correspondence: hshin@gwnu.ac.kr

check for updates

Featured Application: The flange length-dependent stress transfer mechanism revealed in this study may serve as a solid background for the design of the split Hopkinson tension bar with a flange and hollow striker. Investigation of the transfer mechanism also reveals that there exists a case where the superposed magnitude of the flange and bar waves is simply the sum of the respective wave magnitudes, despite the area mismatch of the respective wave medium, and no reverberation occurs as the flange wave enters the bar from flange structure. This interesting phenomenon occurs if the flange wave arrives at the impact plane during the period when the flange and bar waves are generated under the influence of the area mismatch. This phenomenon is observed when the impact and reflection surfaces are close, which may also serve as a basis for interpreting the wave interaction and its result (impact-induced deformation) at regions near the free surface of a three-dimensional protective structure.

Abstract: To reveal the stress transfer mechanism of the flange in a split Hopkinson tension bar, explicit finite element analyses of the impact of the hollow striker on the flange were performed across a range of flange lengths. The tensile stress profiles monitored at the strain gauge position of the incident bar are interpreted on a qualitative basis using three types of stress waves: bar (B) waves, flange (F) waves, and a series of reverberation (R_n) waves. When the flange length (L_f) is long (i.e., $L_f > L_s$, where L_s is the striker length), the B wave and first reverberation wave (R_1) are fully separated in the time axis. When the flange length is intermediate ($\sim D_b < L_f < L_s$, where D_b is the bar diameter), the B and F waves are partially superposed; the F wave is delayed, then followed by a series of R_n waves after the superposition period. When the flange length is short ($L_f < \sim D_b$), the B and F waves are practically fully superposed and form a pseudo-one-step pulse, indicating the necessity of a short flange length to achieve a neat tensile pulse. The magnitudes and periods of the monitored pulses are consistent with the analysis results using the one-dimensional impact theory, including a recently formulated equation for impact-induced stress when the areas of the striker and bar are different, equations for the reflection/transmission ratios of a stress wave, and an equation for pulse duration time. This observation verifies the flange length-dependent stress transfer mechanism on a quantitative basis.

Keywords: impact; wave interaction; reverberation; reflection; transmission; general impedance

1. Introduction

The split Hopkinson bar [1] has been widely used for extracting material properties such as the parameters of strain rate-dependent constitutive models [2,3] which, in turn, are used for the simulation of high strain–rate events such as high-speed transportation crashes, high-speed machining, rock/building blasts, blast impacts, earthquake impacts, ricochets and penetrations [4–7], and explosions. While the original inception of the split Hopkinson bar was based on the compressive mode [1,8–11], modifications have been made thereafter, including the split Hopkinson tension bar (SHTB). The SHTB measures the stress–strain and strain rate–strain curves of versatile materials at strain rates of approximately 400–2000 s^{-1}. The specimen materials include metals, soft materials such as foams and elastomers, and civil engineering materials [12,13] such as cement-based composites, rocks, and (reinforced) concrete.

To obtain the tensile pulse in the SHTB, the technique using a hollow cylinder and flange is probably the most widely employed [14–45]. The schematic of the SHTB system that employs a hollow cylinder and flange is shown in Figure 1.
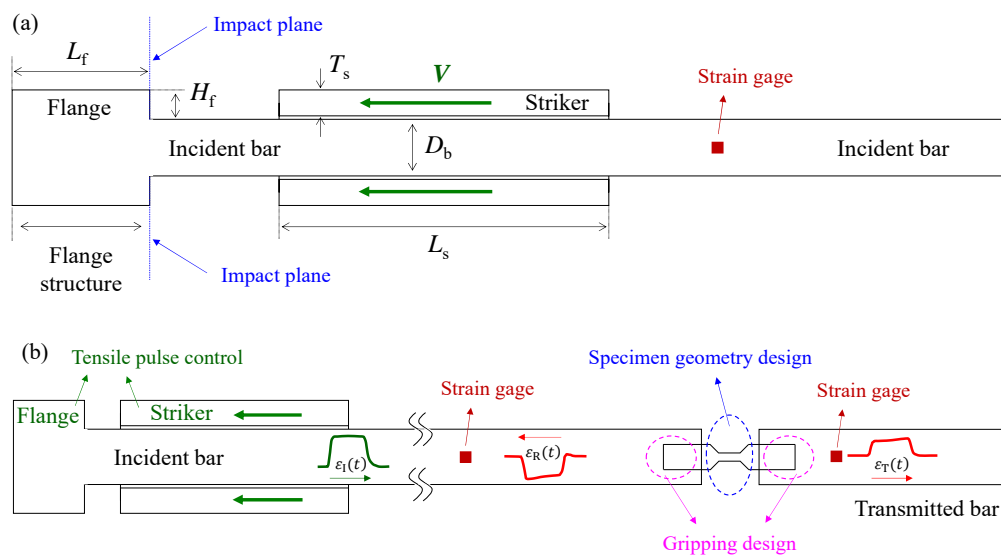
Figure 1. Schematic of: (**a**) hollow striker, flange, and incident bar (L_f: flange length, H_f: flange height, T_s: striker thickness, L_s: striker length, D_b: bar diameter, and V: impact velocity) and (**b**) the overall SHTB system, where ε_I, ε_R, and ε_T denote the incident, reflected, and transmitted pulses, respectively, with time (t).

Briefly, the operation principle of the SHTB is sketched in Figure 1; the hollow striker impacts the flange at velocities of approximately 10–30 m/s. Although the detailed stress transfer mechanism is unknown (revealing the mechanism is the object of this study), it is generally believed that the impact-generated compressive stress wave reflects at the rear (left) end of the flange structure to a tensile stress wave. The reflected tensile wave then travels backwards through the flange structure and enters the incident bar. When this tensile stress wave (ε_I; incident wave) reaches the right end of the incident bar, where the specimen is attached, a part of the tensile stress wave is reflected back to the incident bar as a compressive wave (ε_R), while the rest of it passes through the specimen to enter the transmitted bar as a tensile wave (ε_T).

The transmitted stress wave (ε_T) is measured using a strain gauge, from which the nominal stress of the specimen (σ) is obtained using Equation (1). The nominal strain rate ($\dot{\varepsilon}$) and strain (ε) of the specimen can be obtained most accurately from images of the deforming specimen obtained using an ultra-high speed camera and based on the digital image correlation method. Provided that the designs of specimen geometry, gripping method, and tensile pulse shape are calibrated, the strain

rate ($\dot{\varepsilon}$) and strain (ε) of the specimen can be obtained from the reflected strain pulse (ε_R) measured at the incident bar using the strain gauge; Equations (2) and (3) are used for such purpose. In the case of the split Hopkinson pressure bar (SHPB), Equations (2) and (3) use the reflected pulse (ε_R) and are generally employed to measure the nominal strain rate and strain of the specimen, respectively;

$$\sigma(t) = \left(\frac{A}{A_o}\right) E_o \varepsilon_T(t),$$ (1)

$$\dot{\varepsilon}(t) = -2\left(\frac{C_o}{L}\right) \varepsilon_R(t),$$ (2)

$$\varepsilon(t) = -2\left(\frac{C_o}{L}\right) \int_0^t \varepsilon_R(t) dt.$$ (3)

In the above equations [1,8–11], A and L denote the initial cross-sectional area and initial length of the specimen, respectively; A_o and C_o denote the cross-sectional area and sound speeds of the bar, respectively; and t is the time.

In an SHTB test, problems such as specimen design, gripping, and tensile pulse control [14–18] require resolution (see Figure 1b). This study focuses on the tensile pulse control. Control of the tensile pulse is necessary as a neat tensile pulse without any spurious pulses [18] should be used as an incident tensile wave (ε_I). Otherwise, the ε_R and ε_T waves originating from ε_I are hardly unspoiled, thus preventing the extraction of the neat stress–strain and strain rate–strain curves from the SHTB experiment.

The magnitude and shape of the tensile pulse generated by the transfer flange are governed by many design parameters, such as flange height (H_f), flange length (L_f), striker thickness (T_s), and bar diameter (D_b). In the literature [18], a flange length comparable to the bar diameter has been found to be beneficial. However, the detailed mechanism of how the impact-induced compressive stress is transferred to the tensile stress through the flange structure has not been explored. If the stress transfer mechanism through the flange structure is uncovered, it may aid not only in understanding the stress wave interaction in the SHTB system for design purposes, but also in designing various impact protection structures.

Considering the above, this study investigates the stress transfer mechanism of the flange. For this purpose, the pulse shapes at the strain gauge position of the incident bar are systematically monitored across a range of flange lengths (from D_b to $50D_b$), through an explicit finite element analysis. The monitored tensile stress profiles are interpreted using the three types of waves proposed in this paper: bar waves, flange waves, and a series of reverberation waves. Thereafter, the one-dimensional theory of impact is employed to verify the interpretation, which establishes the flange length-dependent stress transfer mechanism. A positive sign is assigned to the tensile property.

2. Methods

Explicit finite element analysis [46–49] was carried out using a commercial finite element package (Abaqus/Explicit) [50] as the solver. The incident bar and flange of the SHTB were modelled as a single-piece solid body without a specimen and transmission bar. The striker was modelled as a separate solid body. The bar length, measured from the flange end (impact surface) to the free end for specimen contact, was 2000 mm. The gap between the inner surface of the hollow striker and outer surface of the bar was 0.01 mm. The striker was initially 0.1 mm away from the flange (impact surface). The initial velocity of the striker was set as 15 m/s.

Two bar diameters (D_b) were considered: 10 and 20 mm. The flange heights (H_f) were 2.071 and 4.142 mm, respectively, to make the cross-sectional area ratios of the flange to bar unity for both bar diameters (10 and 20 mm). To achieve a neat tensile pulse in the incident bar, the striker thickness (T_s) was the same as the flange height (H_f) [18]; the cross-sectional areas of the flange (A_f) and hollow striker (A_s) were the same. The case where A_s (=A_f) = $0.5A_b$ was also modelled, as a control case.

Half of the two-dimensional axisymmetric geometry was modelled considering the symmetry of the model. The geometry of the model was discretised using four-node bilinear axisymmetric quadrilateral elements (CAX4R). When the mesh sensitivity was tested separately using mesh sizes less than approximately 1×1 mm^2 (radial $\times$ axial dimensions), the stress profile monitored at the strain gauge position exhibited no appreciable change. Based on this result (not shown here), the element size of approximately 0.5×0.5 mm^2 was employed herein for the flange, striker, and bar. An example of the finite element model near the flange structure region is presented in Figure 2.
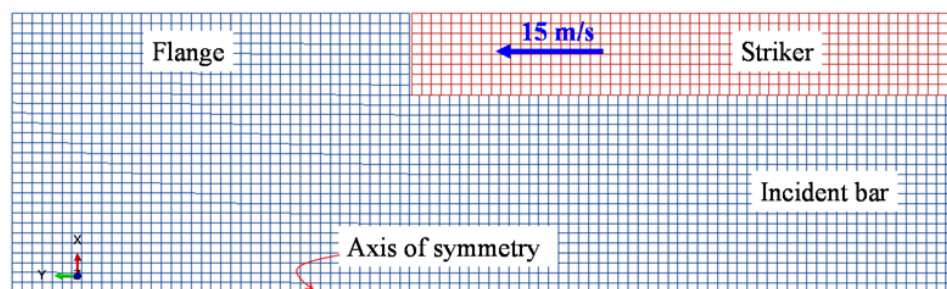
Figure 2. Finite element model near the flange structure region for the case where $A_s/A_b = 1$, $A_s = A_f$, $L_f = 20$ mm, and $D_b = 20$ mm.

The kinematic contact condition was applied to the master–slave contact pair, set for the impact surfaces of the striker and flange. Friction between the contact surfaces was not considered. The solver utilises the central difference time integration method. To ensure solution stability, a stable time increment for each time integration was calculated by the solver by considering the wave speed and minimum element length.

While versatile bar materials such as magnesium, aluminium, titanium alloy, and steel are used in contemporary SHTBs, steel was considered in this study. Although the properties of structural steel vary depending on the type and manufacturer, their density, elastic modulus, and Poisson's ratio were selected arbitrarily herein by referring to the properties of various steel grades [51]: 7800 kg/m^3, 210 GPa, and 0.3, respectively. Although the properties were selected as such, the conclusions drawn out in this study based on the linear elastic analysis are believed to be applicable to the aforementioned bar materials, as well [52]. As all parts of the SHTB model deform elastically, plastic deformation was not considered.

In the post-processing stage, the axial stress component (σ_{yy}) in the incident bar was extracted from a surface element at 1000 mm in the incident bar to avoid the interaction with the reflected wave from the free end of the bar at the specimen side. In experiment setups, the axial strain is usually measured at such a strain gauge position.

3. Results and Discussion

3.1. Stress Contours around Flange Structure

Contours of the axial stress component around the flange structure are shown in Figure 3 for the finite element model presented in Figure 2. As can be observed in Figure 3a, shortly after the striker impact (1.375 µs), both the compressive and tensile stresses form simultaneously in the flange and incident bar, respectively. The compressive wave travels towards the left and right sides of the impact plane. The tensile stress enters the incident bar portion from the moment of impact before the impact signal reaches the left end of the structure, where the compressive stress reflects to a tensile wave. Unlike the contour in Figure 3a (1.375 µs), the contours at 3.392 µs (Figure 3b), 5.337 µs (Figure 3c), and other later moments (not shown) are fairly complicated; the stress transfer mechanism in the flange structure can hardly be investigated solely using such complicated contour diagrams. Therefore, with the notion of the observation in Figure 3a, we investigated the mechanism using

the stress profiles monitored at the strain gauge position of the incident bar (next section), which is usually measured experimentally.
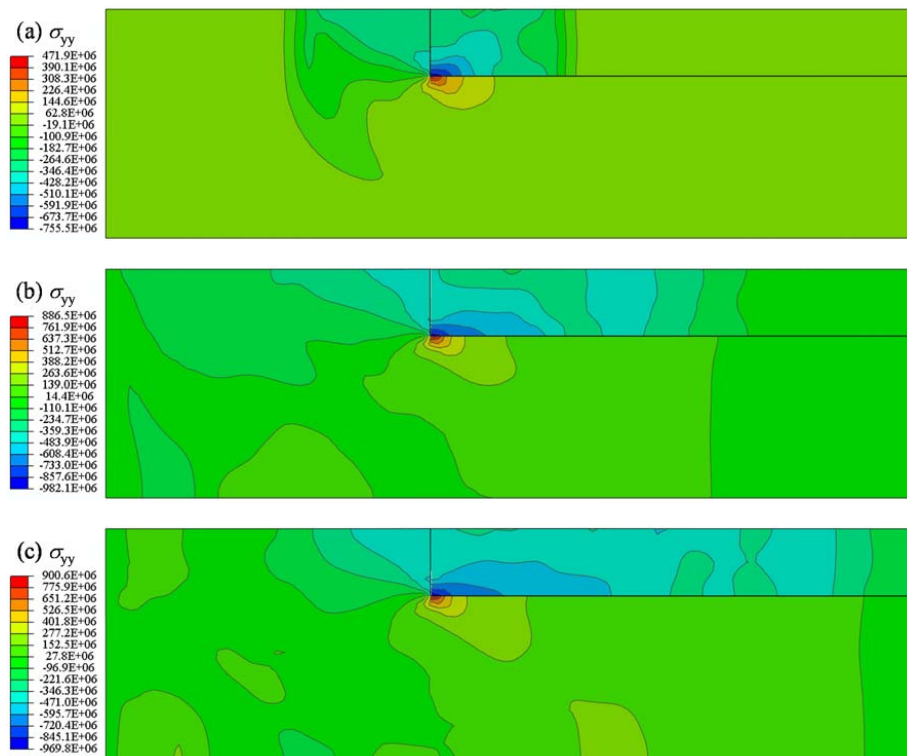
Figure 3. Contours of the axial stress component (σ_{yy}) around the flange structure region for the finite element model shown in Figure 2: (**a**) 1.375, (**b**) 3.392, and (**c**) 5.337 μs after the striker impact. The unit in the legend is Pa.

3.2. Stress Profiles at Strain Gage of Incident Bar

The stress profiles monitored at the strain gauge position in the incident bar over a range of flange lengths (L_f) are presented in Figure 4. In Figure 4a (D_b = 10 mm; A_s/A_b = 1.0), the case where $L_f = D_b$ (black curve) yields a single (pseudo-one-step) tensile pulse starting at approximately 0.19 ms. However, two-step pulses are monitored when $2D_b \leqq L_f \leqq 10D_b$. The reason for this observation is explained below.

When $2D_b \leqq L_f \leqq 10D_b$, the first stress pulse rise is identical to that when $L_f = D_b$, while the second rise starts later (as L_f increases). Focusing on the plateau region after the first rise in the stress signal, the peaks and valleys in the plateau region are identical for different L_f values before the second rise starts. When the pulse duration ends, the tensile pulse also decays in a stepwise manner; such stepwise decay starts later as L_f increases.

When L_f is $50D_b$ (purple curve), two separate tensile pulses appear: the magnitude of the first (marked as **B**) is smaller than that of the second (marked as **R₁**). The definitions of these notations are described in the next section. At a smaller L_f value of $30D_b$ (green curve), the two tensile pulses (**B** and **R₁**) are on the verge of separation.

In Figure 4b (D_b = 20 mm; A_s/A_b = 1.0), as L_f increases up to $10D_b$, the exhibited pulse magnitudes are the same as those in Figure 4a (D_b = 10 mm; A_s/A_b = 1.0). However, at a given L_f value ($2D_b \leqq L_f \leqq 10D_b$), the rise in the second step starts later in Figure 4b than that in Figure 4a. For the case where $L_f = 30D_b$ (green curve), the first (**B**) and second (**R₁**) tensile pulses have already separated; this observation differs from the case in Figure 4a. When $L_f = 50D_b$ (purple curve), the starting time of the second tensile pulse (**R₁**) is further delayed and superposed on the compressive pulse from the free end on the right side of the incident bar.

(**a**)

(**b**)

(**c**)
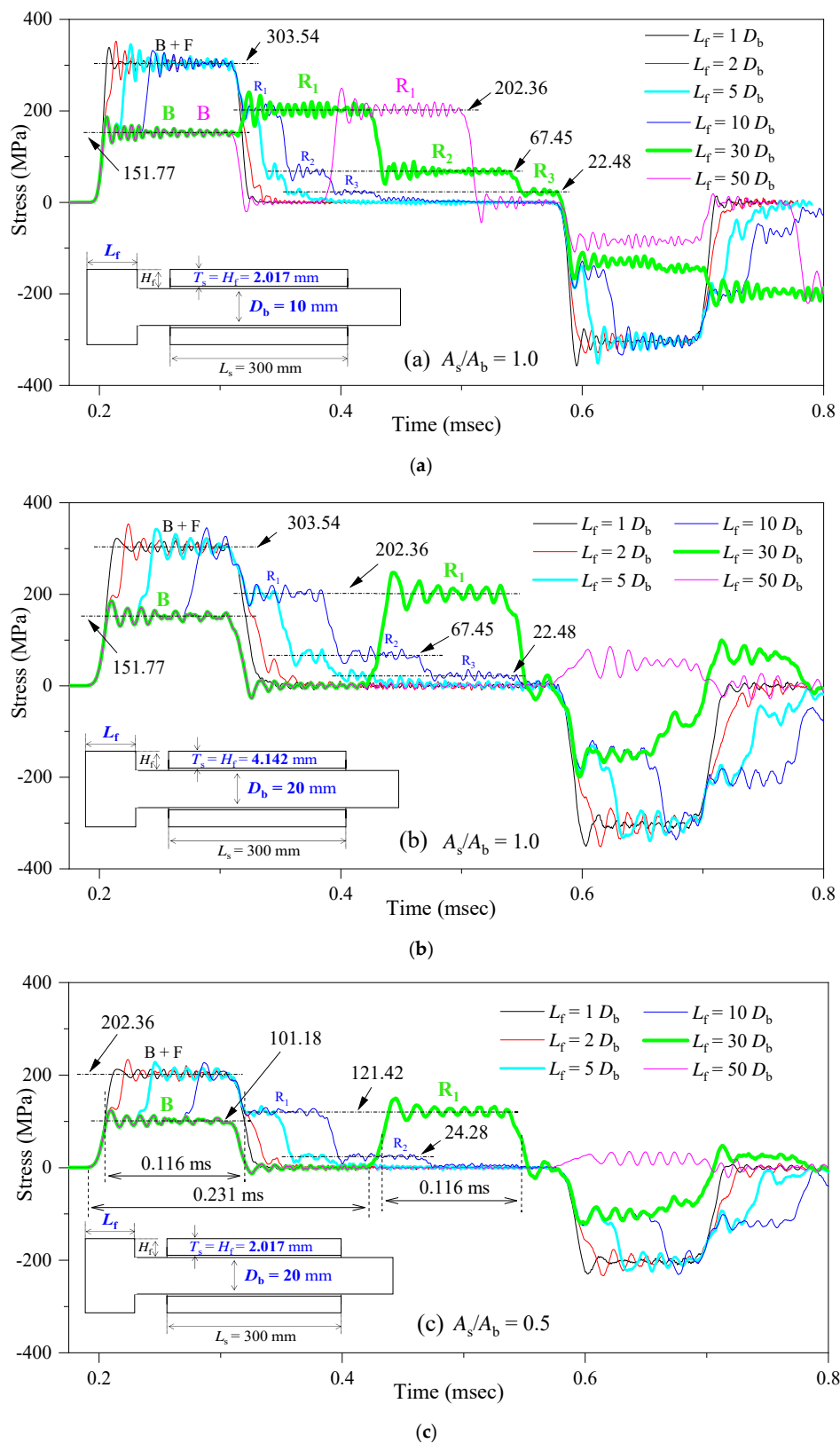
Figure 4. Axial stress (σ_{yy}) profiles observed at the strain gauge position for a range of flange lengths (L_f) at bar diameters (D_b) of: (**a**) 10 mm ($A_s = A_b$), (**b**) 20 mm ($A_s = A_b$), and (**c**) 20 mm ($A_s = 0.5A_b$).

The pulse shapes when D_b = 20 mm and A_s/A_b = 0.5 are presented in Figure 4c. The pulse heights in Figure 4c are diminished compared with those in Figure 4b. The height reduction from 303.24 to

202.36 MPa is explained on a quantitative basis later (see Section 3.4.1), using Equation (4). The rise and decay of the pulses with time in Figure 4c are similar to those in Figure 4b.

3.3. Three Types of Stress Waves

To aid in the interpretation of the stress profiles shown in Figure 4, some terminology is defined, first using the schematic of the flange/bar structure in Figure 5, which was originally prepared to illustrate the three stress waves (**B, F,** and **R$_n$**) proposed in this study. The term "corner" is the right angle between the impact surface on the flange and the outer surface of the bar. The "reference plane" refers to the imaginary radial plane that passes through the impact plane (see Figure 1a). The "flange structure" and "incident bar" are the structures on the left and right sides of the reference plane, respectively. The critical plane (p_c) is the nearest radial plane to the reference plane, after which a homogenised stress state appears. The concept of a critical plane is based on Saint-Venant's principle [53,54].
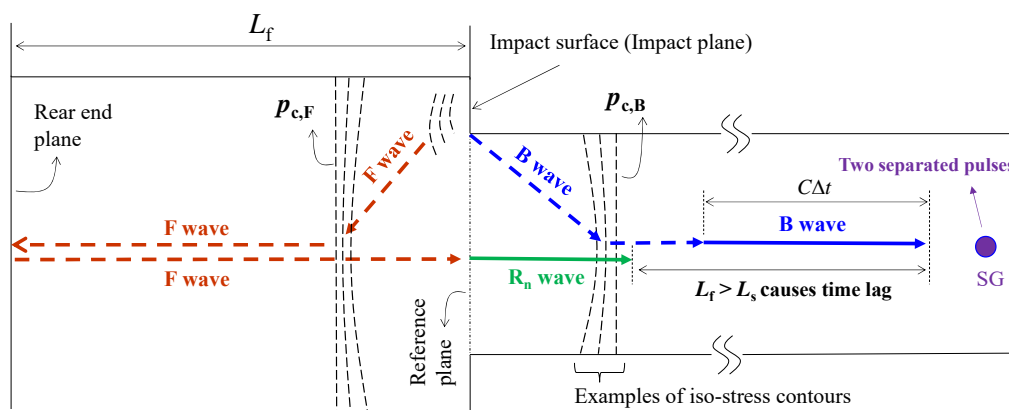
Figure 5. **B, F,** and **R$_n$** waves when the flange length is long ($L_f > L_s$). The solid arrows indicate the waves in the current moment, whereas the dashed arrows describe their trajectories. For simplicity, the **R$_n$** waves in the flange structure are not shown (Δt: pulse duration period, C: speed of sound, and SG: strain gage).

To interpret the monitored stress profiles in the incident bar, three types of stress waves are proposed, as follows. When the hollow striker impacts the flange, the particles on the flange surface (impact surface) move backwards and generate tensile stress on the right side of the reference plane (i.e., in the incident bar, particularly near the corner region). In this study, this generated wave is called the bar wave (**B** wave), as shown in Figure 5. The backward movement of flange particles also generates compressive stress—referred to as the flange wave (**F** wave)—on the left side of the reference plane (i.e., in the flange structure). According to Saint-Venant's principle, both the **B** and **F** waves are homogenised across the radial plane after travelling certain axial distances in the incident bar and flange structure, respectively; the schematic of their critical planes are shown in Figure 5 ($p_{c,B}$ and $p_{c,F}$, respectively).

The compressive **F** wave is reflected at the rear end of the flange structure as a tensile wave, followed by its arrival at the reference plane. When the **F** wave arrives at the reference plane, the reverberation phenomenon is anticipated to occur as follows. If an elastic wave (e.g., the **F** wave) approaches a stress-free interface (e.g., the stress-free reference plane), due to the mismatch in general impedance [52,55], only a part of the stress wave is transmitted to the incident bar, while the rest is reflected back to the flange structure. Accordingly, the residual **F** wave travels back and forth along the flange structure (reverberation takes place), causing it to enter the incident bar multiple times. For convenience, the magnitudes of transmitted waves into the incident bar in the first, second, and third instances of reverberation are denoted as **R$_1$**, **R$_2$**, and **R$_3$**, respectively. These reverberation waves are simply denoted as **R$_n$** waves. As shown in subsequent sections, there are cases where the **F** wave simply enters the incident bar without reverberation and propagates towards the strain gauge.

3.4. Stress Transfer Mechanism

3.4.1. Long Flange ($L_f > L_s$)

The schematic of the three waves when the flange is long ($L_f > L_s$) is shown in Figure 4. It depicts that the arrivals of the $\mathbf{R_n}$ waves are delayed as the $\mathbf{F}$ wave travels a longer distance. Consequently, an overly long flange length certainly leads to separation of the succeeding $\mathbf{R_n}$ wave from the preceding $\mathbf{B}$ wave. According to the one-dimensional theory [52,55], the stress pulse length is $2L_s$ (600 mm) and the travel distance in the flange structure is $2L_f$. Therefore, if $2L_f > 2L_s$ ($L_f > L_s$), then the $\mathbf{F}$ and $\mathbf{R_1}$ waves will separate. In view of this analysis, the long flange length in this study refers to the case where $L_f > L_s$.

For the case where D_b = 10 mm (Figure 4a), the L_s value (300 mm) is $30D_b$. Then, a flange length (L_f) of only $30D_b$ results in the juxtaposition of the $\mathbf{B}$ and $\mathbf{R_1}$ pulses, as shown in Figure 4a, where the $\mathbf{B}$ and $\mathbf{R_1}$ pulses for $L_s = 30D_b$ (green curve) are on the verge of separation. When $D_b = 20$ mm (Figure 4b,c), the L_s value (300 mm) is $15D_b$. Then, when $L_f = 30D_b$ (green curve), two fully separated pulses occur (Figure 4b,c).

Next, the magnitudes of the $\mathbf{B}$ and $\mathbf{R_n}$ waves separated in the time axis are calculated. Note that in Figure 4, the $\mathbf{B}$ and $\mathbf{F}$ waves simultaneously form and propagate in opposite directions. To obtain the proportion at which the impact-generated stress separates into $\mathbf{B}$ and $\mathbf{F}$ waves, the overall magnitude of the impact-generated stress itself should first be determined. For this purpose, a one-dimensional equation [52] that was derived by considering the impact of a cylinder striker on a bar in the compression mode is employed:

$$\sigma_b = \frac{Z_s}{Z_s + Z_b} \rho_b C_b V, \tag{4}$$

where σ is the stress, ρ is the density, C is the sound of speed, z is the general impedance ($A\rho C$), V is the impact velocity, and the subscripts b and s denote the bar and striker, respectively. The magnitudes of the impact-generated stress obtained using Equation (1) when A_s/A_b = 1.0 (Figure 4b) and 0.5 (Figure 4c) are 303.24 and 202.36 MPa, respectively, as indicated by the dash–dot horizontal lines. The vertical positions of the drawn lines are consistent with the plateau height of the first tensile pulse of the case where $L_f = D_b$.

To estimate the proportions of the $\mathbf{B}$ and $\mathbf{F}$ waves in the impact-generated stress magnitude, the plateau heights of the $\mathbf{B}$ wave in the green curves ($L_f = 30D_b$) in Figure 4 are used as a reference (at this point in this discussion, the numbers marked for the plateau of the $\mathbf{B}$ wave are unknown; they are marked in the latter part of this paragraph). In Figure 4, the plateau heights of the $\mathbf{B}$ waves appear to be approximately half of the first tensile pulse when $L_f = D_b$. Based on this observation, the impact-generated stress by the striker—the magnitude of which can be calculated using Equation (4)—is hypothesised to be equally divided between the $\mathbf{B}$ and $\mathbf{F}$ waves. Under this assumption, the calculated magnitudes of the $\mathbf{B}$ and $\mathbf{F}$ waves are 151.77 (A_s/A_b = 1.0; Figure 4b) and 101.18 MPa (A_s/A_b = 0.5; Figure 4c), respectively. The calculated half-magnitudes based on this hypothesis are marked on the first pulse ($\mathbf{B}$ wave) of the green curves ($L_f = 30D_b$) using dash–dot horizontal lines. The vertical positions of the drawn lines are reasonably consistent with the plateau height of the first pulse ($\mathbf{B}$ wave), verifying the hypothesis that the impact-generated stress wave is equally divided between the $\mathbf{B}$ and $\mathbf{F}$ waves. This hypothesis is further verified below.

Consider the case where only the $\mathbf{F}$ wave enters the reference plane after separating from the antecedent $\mathbf{B}$ wave due to the long flange length. The ratios of reflection (R_r) and transmission (R_t) at a stress-free interface are given by [55]:

$$R_r = \frac{\sigma_r}{\sigma_i} = \frac{Z_2 - Z_1}{Z_1 + Z_2}, \tag{5}$$

$$R_t = \frac{\sigma_t}{\sigma_i} = \frac{2A_1 \rho_2 C_2}{Z_1 + Z_2}, \tag{6}$$

where the subscripts i, r, and t denote the incident, reflected, and transmitted waves, respectively; and the subscripts 1 and 2 indicate the incident and transmitted wave media (flange structure and incident bar), respectively.

Starting from an **F** wave magnitude of 151.77 MPa (i.e., the hypothesised value) in Figure 4a (D_b = 10 mm), the magnitudes of the first, second, and third waves transmitted into the incident bar were calculated, using Equations (5) and (6), as 202.36, 67.45, and 22.48 MPa, respectively, as indicated by the dash–dot horizontal lines in Figure 4a. In Figure 4a (D_b = 10 mm), the vertical positions of the drawn lines are found to be consistent with the plateau heights of the first three R_n waves on the green curve (L_f = 30D_b). In Figure 4b (D_b = 20 mm), the plateau height of the first R_n wave (R_1) on the green curve (L_f = 30D_b) is consistent with the drawn line at 202.36 MPa. Finally, in Figure 4c (D_b = 20 mm; A_s/A_b = 0.5), starting from an **F** wave magnitude of 101.18 MPa (hypothesised value), the magnitude of the first R_n wave (R_1) was calculated to be 121.42 MPa. In Figure 4c, this value is also consistent with the plateau height of the R_1 wave for L_f = 30D_b.

The consistency of the various calculation results for the R_1, R_2, and R_3 waves was verified in the previous paragraph under the hypothesis that the impact-generated stress (303.54 and 202.36 MPa for the cases where A_s/A_b = 1.0 and 0.5, respectively) is equally divided between the **B** and **F** waves. Based on verification of the hypothesis, the tensile **B** and compressive **F** waves that simultaneously form are interpreted to be the counterparts of each other across the impact plane; for instance, in the law of action and reaction, if the B wave is the action, then the F wave is the reaction.

The interpretation that two separated pulses on the green curves (L_f = 30D_b) in Figure 4b or Figure 4c (D_b = 20 mm) can be ascribed to the **B** and **F** waves in sequence can be verified from the view of the time lag to the second pulse from the first one. According to Figure 5, the travel distance of the **F** + R_1 wave is longer than that of the **B** wave by 2L_f (=60D_b). The time lag of the **F** wave is then 2L_f/C, which is 0.231 ms. This time interval is marked on the green curve (L_f = 30D_b) in Figure 4c; the positioned mark is reasonably consistent with the time gap of the two separated pulses on the green curve. This observation also verifies the interpretation that two separated pulses on the green curves (L_f = 30D_b) are attributed to the **B** and **F** waves in sequence.

The duration period (Δt) of the separated **B** and **F** waves on the green curves (Figure 4b,c) should be the same as that in the one-dimensional theory [52,55]:

$$\Delta t = 2L_s/C, \tag{7}$$

which results in the duration period (Δt) of 0.116 ms. This time interval (0.116 ms) is marked on the **F** wave in Figure 4c; this mark is reasonably positioned at the full width at half maximum (FWHM) of the **F** wave. This mark is not marked on the **B** wave, as the same time interval (0.116 ms) was already marked to the FWHM of the pseudo-one-step pulse in Figure 4c. If this mark for the pseudo-one-step pulse is shifted to the left side a little bit, the mark can be reasonably positioned at the FWHM of the **B** wave as well (not shown). Therefore, the pulse width of the fully separated **B** and **F** waves is also consistent with the one-dimensional theory of impact.

3.4.2. Intermediate Flange (~D_b < L_f < L_s)

The L_s value (300 mm) corresponds to 30D_b and 15D_b for D_b = 10 and 20 mm, respectively; hence, this section for the intermediate flange length (~D_b < L_f < L_s) focuses on the stress curves for L_f = 2D_b, 5D_b, and 10D_b in Figure 4b,c. The schematic of the **B, F,** and R_n waves in this case is shown in Figure 5.

In the case of a long flange (L_f > L_s) where only the **F** wave enters the incident bar without the influence of the **B** wave, the magnitude of the **F** wave is amplified according to Equation (4) (The amplitude of the transmitted tensile wave is magnified as the reflected wave from the reference plane is compressive. Particles move to the left direction at both the left and right sides of the reference plane during the passage of the stress wave). If the **F** wave approaches the reference plane within

Δt while the **B** wave is being generated, Equations (5) and (6) cannot be applied to the **F** wave; these equations can only be applied to a case where a stress wave reaches a stress-free interface [52,55]. Figure 5 shows that, once the **F** wave meets the **B** wave at the reference plane (after they are superposed), the plateau height in the superposition period appears to simply be the sum of the **B** and **F** waves; the magnitude of the **F** wave is not amplified (i.e., it is not influenced by the area mismatch). This phenomenon occurs because, according to Equation (4), the generation of the **B** wave (action) and **F** wave (reaction) across the impact plane is governed by the cross-sectional area mismatch during the pulse generation period. In other words, the **B** and **F** waves are simply superimposed while they are being generated under the influence of the area mismatch (Equation (4)). Therefore, when the **F** wave enters the reference plane within the pulse period (Δt), the superposed magnitude is simply the sum of **B** and **F** waves, and no reverberation occurs. In such a case, the **F** wave is also defined in the incident bar, as illustrated in Figures 5 and 6.
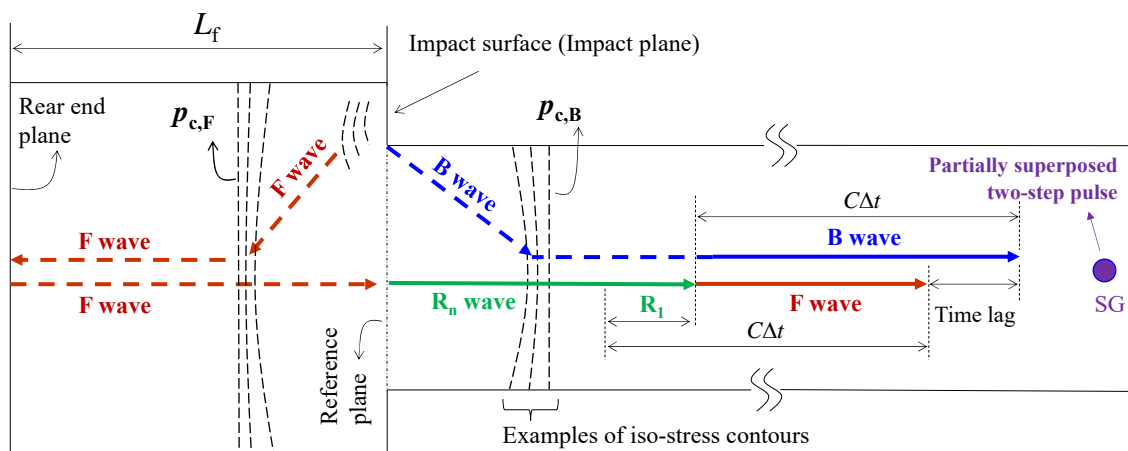
Figure 6. **B, F,** and **R_n** waves when the flange length is intermediate ($\sim D_b < L_f < L_s$). The critical plane for the F wave ($p_{c,F}$) is positioned in the flange structure as L_f, which in this case, is also sufficiently long.

In the case, where the flange length is intermediate ($L_f = 2D_b$, $5D_b$, and $10D_b$ in Figure 4), the first and second wave increases in the stress signal are ascribed to the first-arriving **B** wave and later-arriving **F** wave, respectively. Furthermore, a longer flange increases the travel distance of the **F** wave in the flange structure, delaying the arrival time of the **F** wave. As a result, the second step starts later, and the duration of the superposition decreases with the flange length. All these interpretations are qualitatively consistent with the stress profiles shown in Figure 4.

In the numerical analysis, the same incident bar length (2000 mm) was considered for all flange lengths. Therefore, the discretisation of the incident bar was identical for each FE model, whereas that of the flange structure varies with different FE models, as they have different flange lengths. This is why the average magnitudes, as well as the peaks and valleys of the first plateau region of the tensile pulses (before the second rises) for different curves are identical, although these are from different FE models with various L_f values. The identical peaks and valleys verify that the **B** wave is generated at the right side of the reference plane and travels alone in the incident bar.

After the superposition period, a plateau region which can be solely ascribed to the **F** wave appears in Figure 4. This plateau is the un-superposed latter part of the **F** wave that approaches the reference plane alone (i.e., without the influence of the **B** wave). This latter plateau period of the **F** wave decreases with the flange length, as the arrival of the **F** wave is further delayed. After the superposition period is over, the delayed **F** wave enters the incident bar for the first time to form the first-transmitted **R_n** (**R_1**) wave. Indeed, there are also second and third **R_n** waves transmitted (i.e., **R_2** and **R_3,** respectively) for the intermediate flanges after the **R_1** wave. The magnitudes of **R_1, R_2,** and **R_3** waves were previously calculated when long flanges ($L_f = 30D_b$) were considered. The results are marked in Figure 4b (202.36, 67.45, and 22.48 MPa) and Figure 4c (121.42 and 24.28 MPa), respectively.

The magnitude of the pseudo-one-step pulse was checked in the previous section using Equation (1). Its pulse duration period ($\Delta t = 2L_s/C = 0.116$ ms) is marked in Figure 4c. The calculated result (mark) is reasonably consistent with the FWHM value of the pseudo-one-step pulse.

3.4.3. Short Flange ($L_f < \sim D_b$)

The schematic of the **B** and **F** waves when the flange is short ($L_f < \sim D_b$) is shown in Figure 7. The travel distances of these waves in this case approximate each other, due to the short flange length. The reflected **F** wave from the rear end of the flange reaches the impact plane a short time after the waves (**B** and **F**) start generation from the moment of impact; the **F** wave from the flange end reaches the impact plane at an early stage of the pulse generation period. The **F** wave from the flange end enters the incident bar without reverberation, when monitored at the strain gage position, the following **F** wave is practically fully superposed on the slightly prevenient **B** wave, resulting in a pseudo-one-step pulse. This observation indicates the necessity of a short flange length from the viewpoint of obtaining a neat tensile pulse.
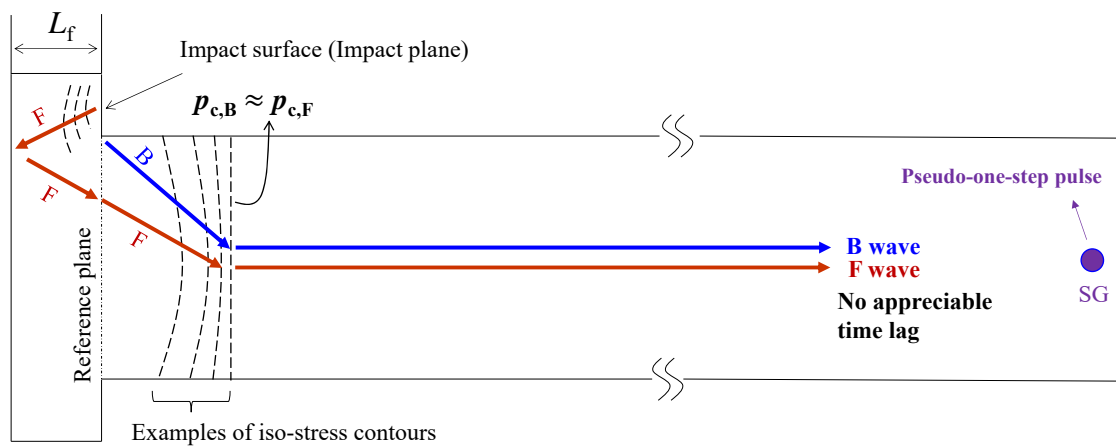
Figure 7. **B** and **F** waves when the flange length is short ($L_f < \sim D_b$), such that the critical plane for the **F** wave ($p_{c,F}$) is positioned in the incident bar and not in the flange structure.

3.5. Overall Discussion

The consistency of the pulse plateau magnitudes (Figure 4) and pulse duration periods (Figure 4c) with the one-dimensional theory (Equations (4)–(7)) discussed in Section 3.4 verifies the flange length-dependent tensile stress mechanism in Section 3.4 on a quantitative basis. The consistency of the numerical analysis results (Figure 4) with the one-dimensional theory (Equations (4)–(7)) also verifies the reliability of the numerical analysis (Section 2) carried out in this study.

The flange length-dependent stress transfer mechanism revealed above may serve as a solid background for the design of SHTBs having a striker and flange. Investigation into the flange length-dependent interactions of the **F** and **B** waves revealed that the superposed magnitude of the **F** and **B** waves is simply the sum the respective wave magnitudes, despite the area mismatch of the respective medium, and that no reverberation occurs as the **F** wave enters the bar from the flange structure with a different cross-sectional area. This interesting phenomenon occurs if the **F** wave arrives at the impact plane before the generation of **F** and **B** waves (which occurs under the influence of area mismatch) is completed. This phenomenon is observed when the impact and reflection surfaces are close, which may also serve as a background for interpreting wave interaction and impact-induced deformation at regions near the free surface of a three-dimensional protective structure.

4. Conclusions

The tensile stress profiles monitored at the strain gauge of the incident bar were interpreted using three types of stress waves: bar (**B**) waves, flange (**F**) waves, and a series of reverberation (**R_n**) waves. When the flange length (L_f) was long ($L_f > L_s$; L_s is the striker length), the reflected **F** wave from the rear end of the flange reached the impact plane after generation of the waves (**B** and **F**) at the impact plane was completed. When the **F** wave entered the incident bar across the impact plane, reverberation occurred in the flange structure due to mismatch of the general impedance at the impact plane. When the signal was measured at the strain gauge position, the first reverberation wave (**R_1**) was fully separated from the **B** wave in the time axis.

When the flange length was intermediate ($\sim D_b < L_f < L_s$; D_b is the bar diameter), the reflected **F** wave from the rear end of the flange reached the impact plane before the simultaneous generation of the waves (**B** and **F**) was finished at the impact plane; this occurred during the period when the waves (**B** and **F**) were being generated at the impact plane. In such a case, the **F** wave coming from the rear end of the flange enters the incident bar across the impact plane without reverberation; the **F** wave is simply superposed to the **B** wave which is being generated, and the superposed magnitude is simply the sum of the interacting waves. When the signal was monitored at the strain gage position, a two-step pulse appeared; the first step was the **B** wave and the second step was the superposed **B** and **F** waves. The magnitude of the second step was twice that of the first step. When the superposition period was over (i.e., when the pulse generation event was over), the rear part of the **F** wave that entered the incident plane experienced reverberation.

When the flange length was short ($L_f < \sim D_b$), the reflected **F** wave from the rear end of the flange reached the impact plane a short time after the waves (**B** and **F**) started generation from the moment of impact; the **F** wave from the flange end reached the impact plane at an early stage of the pulse generation period. As the **F** wave from the flange end entered the incident bar without reverberation, when monitored at the strain gauge position, the following **F** wave was practically fully superposed onto the slightly prevenient **B** wave, resulting in a pseudo-one-step pulse. This observation indicates the necessity of a short flange length, from the view of obtaining a neat tensile pulse.

The magnitudes and duration periods of the pulse plateaus were also analysed using one-dimensional impact theory, including a recently formulated equation for impact-induced stress when the striker and bar areas are different (Equation (4)), equations for the reflection/transmission ratios of a stress wave (Equations (5) and (6)), and an equation for the pulse duration time (Equation (7)). Consistency of the observed pulses with the one-dimensional theory was found, which verified the flange length-dependent stress transfer mechanism on a quantitative basis.

The flange length-dependent stress transfer mechanism revealed above may serve as a solid background for the design of SHTBs. Investigation into the flange length-dependent interactions of the **F** and **B** waves revealed that, if the waves are superimposed while they are being generated under the influence of the area mismatch, the superposed magnitude is simply the sum of the interacting waves, despite the area mismatch, and no reverberation occurred as the **F** wave entered the bar with different cross-sectional area. This phenomenon observed when the impact and reflection surfaces were close may also serve as a background for interpreting wave interactions and its result (impact-induced deformation) at regions near the free surface of a three-dimensional protective structure.

Conflicts of Interest: The authors declare no conflict of interest. The funders had no role in the design of the study; in the collection, analyses, or interpretation of data; in the writing of the manuscript, nor in the decision to publish the results.

References

1. Kolsky, H. An investigation of the mechanical properties of materials at very high rates of loading. *Proc. Phys. Soc. Lond. Sect. B* **1949**, *62*, 676–700. [CrossRef]
2. Johnson, G.R.; Cook, W.H. A constitutive model and data for metals subjected to large strains, high strain rates and high temperatures. In Proceedings of the 7th International Symposium on Ballistics, The Hague, The Netherlands, 19–21 April 1983; pp. 541–547.
3. Shin, H.; Kim, J.-B. A phenomenological constitutive equation to describe various flow stress behaviors of materials in wide strain rate and temperature regimes. *J. Eng. Mater. Technol.* **2010**, *132*, 021009. [CrossRef]
4. Lee, W.; Lee, H.-J.; Shin, H. Ricochet of a tungsten heavy alloy long-rod projectile from deformable steel plates. *J. Phys. D Appl. Phys.* **2002**, *35*, 2676–2686. [CrossRef]
5. Pyka, D.; Kurzawa, A.; Bocian, M.; Bajkowski, M.; Magier, M.; Sliwinski, J.; Jamroziak, K. Numerical and experimental studies of the ŁK type shaped charge. *Appl. Sci.* **2020**, *10*, 6742. [CrossRef]
6. Lu, Y.; Zhang, Q.; Xue, Y.; Liu, W.; Long, R. High-velocity impact performance of aluminum and B_4C/UHMW-PE composite plate for multi-wall shielding. *Appl. Sci.* **2020**, *10*, 721. [CrossRef]
7. Yoo, Y.H.; Paik, S.H.; Kim, J.B.; Shin, H. Performance of a flying cross bar to incapacitate a long-rod penetrator based on a finite element model. *Eng. Comput.* **2012**, *29*, 409–415. [CrossRef]
8. Chen, W.W.; Song, B. *Split Hopkinson (Kolsky) Bar—Design, Testing and Applications*; Springer: New York, NY, USA, 2011.
9. Shin, H.; Kim, J.-B. Evolution of specimen strain rate in split Hopkinson bar test. *Proc. Inst. Mech. Eng. Part C J. Mech. Eng. Sci.* **2019**, *233*, 4667–4687. [CrossRef]
10. Panowicz, R.; Konarzewski, M. Influence of imperfect position of a striker and input bar on wave propagation in a split Hopkinson pressure bar (SHPB) setup with a pulse-shape technique. *Appl. Sci.* **2020**, *10*, 2423. [CrossRef]
11. Shin, H.; Kim, J.-B. Understanding the anomalously long duration time of the transmitted pulse from a soft specimen in a Kolsky bar experiment. *Int. J. Precis. Eng. Manuf.* **2016**, *17*, 203–208. [CrossRef]
12. De Matteis, G.; Brando, G.; Mazzolani, F.M. Pure aluminium: An innovative material for structural applications in seismic engineering. *Constr. Build. Mater.* **2012**, *26*, 677–686. [CrossRef]
13. Curosu, I.; Mechtcherine, V.; Forni, D.; Cadoni, E. Performance of various strain-hardening cement-based composites (SHCC) subject to uniaxial impact tensile loading. *Cem. Concr. Res.* **2017**, *102*, 16–28. [CrossRef]
14. Verleysen, P.; Degrieck, J.; Verstraete, T.; Van Slycken, J. Influence of specimen geometry on split Hopkinson tensile bar tests on sheet materials. *Exp. Mech.* **2008**, *48*, 587–598. [CrossRef]
15. Rotbaum, Y.; Rittel, D. Is there an optimal gauge length for dynamic tensile specimens? *Exp. Mech.* **2014**, *54*, 1205–1214. [CrossRef]
16. Ledford, N.; Paul, H.; Ganzenmüller, G.; May, M.; Höfemann, M.; Otto, M.; Petrinic, N. Investigations on specimen design and mounting for split Hopkinson tension bar (SHTB) experiments. *Eur. Phys. J. Web Conf.* **2015**, *94*, 01049. [CrossRef]
17. Nguyen, K.-H.; Kim, H.C.; Shin, H.; Yoo, Y.H.; Kim, J.B. Numerical investigation into the stress wave transmitting characteristics of threads in the split Hopkinson tensile bar test. *Int. J. Impact Eng.* **2017**, *109*, 253–263. [CrossRef]
18. Shin, H.; Lee, J.-H.; Kim, J.-B.; Sohn, S.-I. Design guidelines for the striker and transfer flange of a split Hopkinson tension bar and the origin of spurious waves. *Proc. Inst. Mech. Eng. Part C J. Mech. Eng. Sci.* **2020**, *234*, 137–151. [CrossRef]
19. Acosta, J.F. Numerical and Experimental Studies on the Use of a Split Hopkinson Pressure Bar for High Strain Rate Tension Testing. Ph.D. Thesis, Department Aerospace Engineering, Wichita State University, Wichita, KN, USA, 2012.
20. Prabowo, D.A.; Kariem, M.A.; Gunawan, L. The Effect of specimen dimension on the results of the split-Hopkinson tension bar testing. *Procedia Eng.* **2017**, *173*, 608–614. [CrossRef]

21. Chen, X.; Liu, Z.; He, G.; Xie, H. A novel integrated tension-compression design for a mini split Hopkinson bar apparatus. *Rev. Sci. Instrum.* **2014**, *85*, 035114. [CrossRef]

22. Ganzenmüller, G.C.; Blaum, E.; Mohrmann, D.; Langhof, T.; Plappert, D.; Ledford, N.; Paul, H.; Hiermaier, S. A simplified design for a split Hopkinson tension bar with long pulse duration. *Procedia Eng.* **2017**, *197*, 109–118. [CrossRef]

23. Isakov, M.; Hiermaier, S.; Kuokkala, V.-T. Improved specimen recovery in tensile split Hopkinson bar. *Philos. Tans. R. Soc. A* **2014**, *372*, 20130194. [CrossRef]

24. Gerlach, R.; Kettenbeil, C.; Petrinic, N. A new split Hopkinson tensile bar design. *Int. J. Impact Eng.* **2012**, *50*, 63–67. [CrossRef]

25. Huang, S.; Chen, R.; Xia, K.W. Quantification of dynamic tensile parameters of rocks using a modified Kolsky tension bar apparatus. *J. Rock Mech. Geotech. Eng.* **2010**, *2*, 162–168. [CrossRef]

26. Miao, Y.; Du, B.; Ma, C.; Hu, H.; Deng, Q. Some fundamental problems concerning the measurement accuracy of the Hopkinson tension bar technique. *Meas. Sci. Technol.* **2019**, *30*, 055009. [CrossRef]

27. Tzibula, S.; Lovingera, Z.; Rittel, D. Dynamic tension of ductile polymers: Experimentation and modelling. *Mech. Mater.* **2018**, *123*, 30–42. [CrossRef]

28. Gerlach, R.; Sathianathan, S.K.; Siviour, C.; Petrinic, N. A novel method for pulse shaping of split Hopkinson tensile bar signals. *Int. J. Impact Eng.* **2011**, *38*, 976–980. [CrossRef]

29. Yang, X.; Xiong, X.; Yin, Z.; Wang, H.; Wang, J.; Chen, D. Interrupted test of advanced high strength steel with tensile split Hopkinson bar method. *Exp. Mech.* **2014**, *54*, 641–652. [CrossRef]

30. Cao, K.; Wang, Y.; Wang, Y. Experimental investigation and modeling of the tension behavior of polycarbonate with temperature effects from low to high strain rates. *Int. J. Solids Struct.* **2014**, *51*, 2539–2548. [CrossRef]

31. Young, K. Development of a Tensile Split Hopkinson Pressure Bar Testing Facility. Master's Thesis, Department of Mechanical, Automotive and Materials Engineering, Windsor University, Windsor, ON, Canada, 2015.

32. Suga, K.; Okamotob, K.; Takagi, K.; Nakatani, H.; Ogihara, S.; Kikuchi, M. Numerical validation of split Hopkinson pressure bar technique for evaluating tensile mechanical properties of CFRP laminates. *Adv. Compos. Mater.* **2012**, *21*, 21–232. [CrossRef]

33. Guzman, O.; Frew, D.J.; Chen, W.A. Kolsky tension bar technique using a hollow incident tube. *Meas. Sci. Technol.* **2011**, *22*, 045703. [CrossRef]

34. Lim, J.; Chen, W.W.; Zheng, J.Q. Dynamic small strain measurements of Kevlar 129 single fibers with a miniaturized tension Kolsky bar. *Polym. Test.* **2010**, *29*, 701–705. [CrossRef]

35. Owens, A.T.; Tippur, H.V. A Tensile split Hopkinson bar for testing particulate polymer composites under elevated rates of loading. *Exp. Mech.* **2009**, *49*, 799–811. [CrossRef]

36. Fu, S.; Wang, Y.; Wang, Y. Tension testing of polycarbonate at high strain rates. *Polym. Test.* **2009**, *28*, 724–729. [CrossRef]

37. Naik, N.K.; Perla, Y. Mechanical behaviour of acrylic under high strain rate tensile loading. *Polym. Test.* **2008**, *27*, 504–512. [CrossRef]

38. Owens, A.T. Development of a Split Hopkinson Tension Bar for Testing Stress–Strain Response of Particulate Composites under High Rates of Loading. Master's Thesis, Department of Mechanical Engineering, Auburn University, Auburn, AL, USA, 2007.

39. Huh, H.; Kang, W.J.; Han, S.S. Tension split Hopkinson bar for investigating the dynamic behavior of sheet metals. *Exp. Mech.* **2002**, *42*, 8–17. [CrossRef]

40. Chen, W.; Lu, F.; Cheng, M. Tension and compression tests of two polymers under quasistatic and dynamic loading. *Polym. Test.* **2002**, *21*, 113–121. [CrossRef]

41. Li, M.; Wang, R.; Han, M.-B. A Kolsky Bar: Tension, Tension-tension. *Exp. Mech.* **1993**, *33*, 7–14. [CrossRef]

42. Nemat-Nasser, S.; Isaacs, J.B.; Starrett, J.E. Hopkinson techniques for dynamic recovery experiments. *Proc. R. Soc. A* **1991**, *435*, 371–391.

43. Ogawa, K. Impact-tension compression test by using a split-Hopkinson bar. *Exp. Mech.* **1983**, *24*, 81–86. [CrossRef]

44. Harding, J.; Wood, E.O.; Campbell, J.D. Tensile testing of materials at high rates of strain. *Exp. Mech.* **1981**, *21*, 177–185.

45. Nguyen, K.H.; Lee, C.-W.; Shin, H.; Lee, J.H.; Kim, J.-B. A study on the effects of specimen geometry on measurement accuracy of dynamic constitutive properties of metals using SHTB. *Int. J. Precis. Eng. Manuf.* **2020**, *21*, 1687–1695. [CrossRef]

46. Paslar, N.; Farzampour, A.; Hatami, F. Infill plate interconnection effects on the structural behavior of steel plate shear walls. *Thin-Walled Struct.* **2020**, *149*, 106621.

47. Farzampour, A.; Eatherton, M.R. Parametric computational study on butterfly-shaped hysteretic dampers. *Front. Struct. Civ. Eng.* **2019**, *13*, 1214–1226.

48. Mansouri, I.; Arabzadeh, A.; Farzampour, A.; Hu, J.W. Seismic behavior investigation of the steel multi-story moment frames with steel plate shear walls. *Steel Compos. Struct.* **2020**, *37*, 91–98.

49. Farzampour, A.; Khatibinia, M.; Mansouri, I. Shape optimization of butterfly-shaped shear links using grey wolf algorithm. *Ing. Sismica* **2019**, *36*, 27–41.

50. Dassault Systèmes. *Abaqus Analysis User's Manual (Abaqus 6.14)*; © Dassault Systèmes: Vélizy-Villacoublay, France, 2014.

51. MatWeb, Material Property Data. Available online: http://www.matweb.com/ (accessed on 28 October 2020).

52. Shin, H.; Kim, D. One dimensional analyses of striker impact on bar with different general impedance. *Proc. Inst. Mech. Eng. Part C J. Mech. Eng. Sci.* **2020**, *234*, 589–608.

53. Punmia, B.C.; Jain, A.K.; Jain, A.K. *Mechanics of Materials*; Laxmi Publications, Ltd.: New Delhi, India, 2001.

54. Kim, D.; Shin, H. Minimum required distance of strain gauge from specimen for measuring transmitted signal in split Hopkinson pressure bar test. *MATEC Web Conf.* **2020**, *308*, 04005.

55. Meyers, M.A. *Dynamic Behavior of Materials*; John Wiley & Sons, Inc.: New York, NY, USA, 1994.